Engineering Structures 240 (2021) 112367

Contents lists available at ScienceDirect

Engineering Structures

journal homepage: www.elsevier.com/locate/engstruct

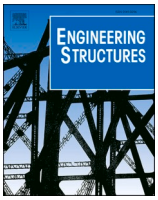

A theoretical study of the dynamic response of planar timber frames with semi-rigid moment-resisting connections subjected to wind loads

Alex Sixie Cao [a,b,*], Haris Stamatopoulos [a]

[a] Department of Structural Engineering, Norwegian University of Science and Technology (NTNU), Richard Birkelands vei 1A, 7491 Trondheim, Norway
[b] Institute of Structural Engineering, ETH Zurich, Stefano-Franscini Platz 5, 8093 Zurich, Switzerland

ARTICLE INFO

Keywords:
Moment-resisting timber frames
Semi-rigid connections
Wind-induced vibrations
Time-domain analysis
Frequency-domain analysis
Serviceability in timber frames
Tall timber buildings

ABSTRACT

The dynamic response of semi-rigid timber frames subjected to wind loads is investigated numerically in this paper. The dynamic response of more than one million unique frames with different parameters was assessed with the frequency-domain gust factor approach, which is currently adopted by Eurocode 1, and the time-domain generalized wind load method. In the generalized wind load method, the frames were simulated for three different wind velocities with five simulations per unique combination of parameters, resulting in more than twelve million simulations in total. Qualitative and quantitative observations of the dataset were made. Empirical expressions for the accelerations, displacements, and fundamental eigenfrequency were proposed by the use of nonlinear regression applied to the obtained numerical results and a frequency reduction factor was developed. The wind-induced accelerations obtained by the two methods were compared to the corresponding serviceability criteria according to ISO10137, providing insight about the feasibility of moment-resisting frames as a lateral load-carrying system for mid-rise timber buildings. Comparison between the theoretical gust factor approach and the generalized wind load method showed that the gust factor approach was nonconservative in most cases. Finally, the effect of uniform and non-uniform mass distributions was investigated, with a theoretical reduction in top-floor accelerations of 50% and 25% respectively.

1. Introduction

Timber structures are lightweight and flexible compared to structures built with other traditional materials such as steel and concrete. Because of these properties, timber structures are subjected to smaller forces due to earthquakes [1,2] and result in smaller forces in the foundations. However, the lightness and flexibility of timber structures make them prone to dynamic loads in the serviceability limit state. Some examples are wind-induced vibrations [3], vibrations from metros [4,5], human-induced vibrations [6,7], and other sources of dynamic loads. For tall timber buildings, wind-induced accelerations are often the limiting factor, which governs the design [8–11]. Buildings that are considered tall when built in timber, are most often considered as mid-rise structures when built in steel or concrete. However, such structures are at the frontier of timber engineering where wind-induced vibrations are an important design consideration.

At present, connections with dowel-type fasteners loaded perpendicular to their axis are very common in timber engineering. Such laterally loaded fasteners feature low stiffness and require minimum end and edge distances. Consequently, it may be a challenge to achieve the desired rotational stiffness in connections with laterally loaded fasteners, even if many fasteners and shear planes are used [12]. Laterally loaded fasteners also show nonlinearities for low rotations due to initial slip. This may compromise their performance for the serviceability limit state.

Tall timber buildings are typically built with either cross-laminated timber (CLT) or glued laminated timber (glulam) elements with extensive trusswork bracing systems. Buildings with CLT elements are less flexible with respect to change in area use, as most of the wall elements are load bearing with short-span deck elements. Buildings with glulam elements require extensive bracing systems. These bracings are often quite massive, which can be witnessed in the record projects Mjø'stårnet [13] and Treet [14]. Therefore, structural systems based on both CLT and glulam trusswork result in architectural restrictions with respect to spatial flexibility. As an alternative to buildings with CLT or glulam trusswork bracing, moment-resisting timber frames with semi-rigid connections can be used as a lateral load-carrying system in mid-rise timber buildings. This will allow for greater architectural flexibility.

* Corresponding author at: Chair of Structural Engineering – Timber Structures, ETH Zürich, Switzerland.
E-mail addresses: cao@ibk.baug.ethz.ch (A.S. Cao), haris.stamatopoulos@ntnu.no (H. Stamatopoulos).

https://doi.org/10.1016/j.engstruct.2021.112367
Received 17 November 2020; Received in revised form 22 February 2021; Accepted 4 April 2021
Available online 2 May 2021

As a result of the increased rotational stiffness of the connections, the lateral stiffness of the whole structure will also increase. By increasing the stiffness of the structure, the dynamic response of the structure will become more favorable and taller timber structures can be engineered. Introduction of semi-rigid moment-resisting connections can also enhance the performance of floors against human-induced vibrations, allowing for greater free spans [12].

Today, semi-rigid moment-resisting timber frames are a novelty in their own. Most of the existing semi-rigid timber frames are on the laboratory scale. One such system is the semi-rigid frame system developed by the Norwegian University of Science and Technology as part of the research project Woodsol [15]. The semi-rigid frame system developed in Woodsol consists of continuous glulam columns and composite floor elements connected to the columns with semi-rigid moment-resisting connections. Therefore, the rotational stiffness of the connections and the increased bending stiffness of the composite floors contribute to the overall stiffness of the structural system. The connections consist of screwed-in threaded rods with the threads at an angle to the grain and metallic coupling parts [16]. The threaded rods are used due to their high axial stiffness and capacity, and their ability to take load without initial slip [17]. The composite floors consist of glulam webs and laminated veneer lumber (LVL) panels acting as flanges. This timber floor has also been developed as part of Woodsol, and its static and dynamic properties have been investigated numerically and experimentally on a full-scale prototype [18].

Other typologies of semi-rigid moment-resisting connections include various configurations of glued-in rods parallel to the grain [19], tube-type fasteners [20,21], dowel-type fasteners [22], post-tensioned systems [23], and more. Important problems to solve for timber connections in the serviceability limit state are the lack of rotational stiffness and initial slip [12].

Vilguts, Stamatopoulos and Malo [24] investigated the dynamic properties and response of 17 800 semi-rigid timber frames subject to different wind loads based on the Woodsol system. Timber frames with up to twelve floors were investigated. The peak accelerations were calculated by using the gust factor approach in accordance with EN1991-1-4 [25] and compared with serviceability requirements in ISO10137 [26]. They found that the column stiffness, number of bays, and connections' rotational stiffness had a large impact on the wind-induced acceleration. For the fundamental eigenfrequency, the most important parameters were the total height, depth of the frame, column stiffness, connection stiffness, bay length, and floor height. Vilguts, Stamatopoulos and Malo [24] found that the expressions for the fundamental eigenperiods in EN1998-1 [27] and EN1991-1-4 [25] did not approximate the fundamental eigenfrequencies from FE analysis for moment-resisting timber frames well.

Edskär and Lidelöw [9] investigated wind-induced vibrations on 27 different configurations of a CLT building with 10 to 22 storeys by using the gust factor approach adopted by EN1991-1-4 [28]. They found that the damping ratio is an important parameter and that increased stiffness reduced the accelerations more than increased mass. They also emphasized the importance of carrying out similar analyses for other structural systems in timber buildings. In addition, they suggested that further work should be carried out on the interaction between mass and stiffness on the dynamic properties and response of timber buildings. Bezabeh et al. [8] studied the wind-induced vibrations of five prototype mass-timber buildings with heights from 10 to 40 storeys. They performed scaled wind-tunnel testing on the 40-storey building and dynamic analysis in the frequency-domain. Results from their analyses indicate a strong dependency on the height, damping ratio, and wind conditions. Suggested mitigation strategies from Bezabeh et al. [8] include increasing the damping capacity and the hybridization of timber buildings with steel and reinforced concrete.

Lui and Lopes [29] investigated the effects of connection flexibility in steel frames subject to dynamic loads. They found that reduced connection stiffnesses increased the natural period and that the required time for the structure to reach steady-state vibration after forced excitation was longer than for a rigid frame. Awkar and Lui [30] later investigated the effects of connection stiffness in steel structures subject to seismic loads. They found that low connection stiffnesses reduced the base shear and overturning moment for multistory frames and that the higher modes were largely unaffected by the low connection stiffnesses.

From several measurements of existing timber structures with heights between 20m and 45m, Feldmann et al. [31] found that the approximation of the fundamental eigenfrequency in EN1991-1-4 [25] gives a too high estimate for some of the measured structures. Structures with lower fundamental eigenfrequencies are more susceptible to wind-induced vibrations, making these estimates nonconservative. Johansson, Jarnerö and Landel [11] performed a simplified concept study of a 22-storey structure consisting of glulam and CLT elements. In the concept study, the wind-induced accelerations were compared to the serviceability requirements in ISO10137 [26] according to the gust factor approach in EN1991-1-4 [25]. They found that the peak acceleration did not satisfy serviceability criteria in ISO10137 [26] and that the fundamental eigenfrequency was about 0.6 Hz. In the tall timber structure *Treet* in Norway, the FE model had a fundamental eigenfrequency of 0.75 Hz [10,11]. In both *Treet* and *Mjøstårnet* in Norway, the wind-induced vibrations were on the limit according to ISO10137 [11,13].

Aloisio et al. [32] measured the eigenfrequencies and corresponding damping ratios in an 8-storey CLT building with a CLT core by the use of operational modal analysis for low-level wind loads. They found that the building had a fundamental eigenfrequency of 1.9 Hz with a corresponding damping ratio of 1.2%. The fundamental eigenfrequency is in the same range as concrete structures of similar height. Another interesting finding was that the building behaved as a continuum where the connection stiffnesses were negligible. Reynolds, Casagrande and Tomasi [33] measured the eigenfrequencies and damping ratios for a light timber frame and a CLT building, both with five storeys and concrete cores. Both of the buildings had a fundamental eigenfrequency of around 4.1 Hz and a damping ratio around 6%. The large difference in the measurements between the two buildings may stem from the different materials used in the central core and measurement methods [34].

Based on the composite timber floors and semi-rigid connections in the Woodsol project, this paper extends the work by Vilguts, Stamatopoulos and Malo [24]. It investigates the dynamic properties and response of tall timber structures of semi-rigid planar frames subject to static and dynamic wind loads. The analysis is done through the simulation of more than 1 million unique moment-resisting frames with different parameters subject to different wind loads. In total, more than 12 million simulations were performed. In the simulations, the effect of different stiffness parameters and surface loads on the structural response was assessed. The results of the simulations were utilized to derive empirical expressions for the response accelerations and fundamental eigenfrequencies based on nonlinear regression. Moreover, a novel frequency reduction factor, which shows the effects of the connections' stiffness, was proposed. Finally, the effect of uniform and non-uniform mass distributions was investigated.

The dynamic response was investigated by using both the simplified frequency-domain gust factor approach used in EN1991-1-4 [25], developed by Davenport [43–45] and Solari [47–50] and a theoretical time-domain generalized wind loading method outlined in Kareem [46] and Steenbergen & Vrouwenvelder [51]. To assess the dynamic properties of the timber structures, a MATLAB routine was developed. The developed MATLAB routine computes the dynamic properties of planar semi-rigid timber frames by using the FE method and simulates the dynamic response of the semi-rigid, planar, moment-resisting timber frames from the gust factor approach and the generalized wind load method. In the generalized wind load method, 10-minute time series for the wind loads were generated based on the Kaimal spectrum [35] in EN1991-1-4 [25]. The response accelerations of the frames were

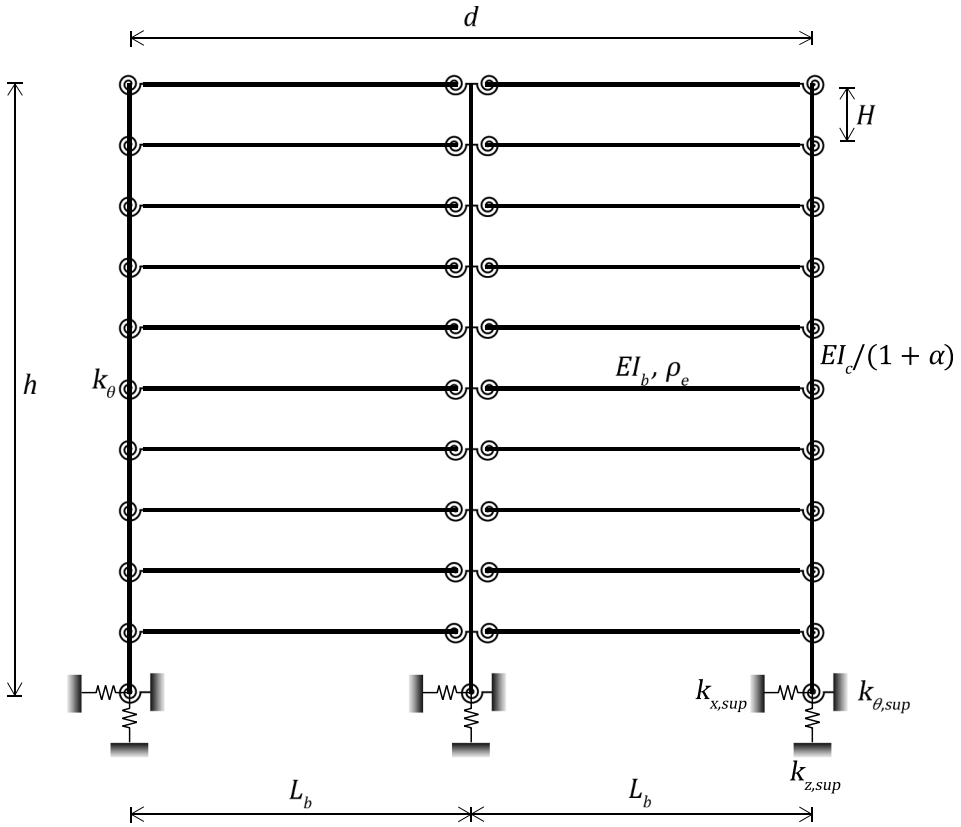

Fig. 1. An arbitrary planar frame with floors n_{floor}, bays n_{bay}, beam stiffness EI_b, beam length L_b, column stiffness EI_c, column length H, connection stiffness k_θ, horizontal support stiffness $k_{x,sup}$, vertical support stiffness $k_{z,sup}$, rotational support stiffness $k_{\theta,sup}$, building depth d, building height h, and an equivalent beam density ρ_e.

compared with the serviceability requirements for wind-induced vibrations in ISO10137 [26].

2. Method

2.1. Finite element formulation

A general layout of the structural system is illustrated in Fig. 1. The system consists of continuous vertical columns and discontinuous horizontal beam elements that represent the composite floors. The beams are connected to the columns by rotational springs with a spring constant k_θ, which represent the moment-resisting connections. The translational Degrees of Freedom (DOF) in the connections are assumed as rigid since they have a small influence on the lateral response of the frames. Timoshenko rectangular beam elements are used for the columns, since the shear deformation in the column elements is significant for the lateral response. The shear coefficient is set to 6/5. Euler-Bernoulli rectangular beam elements with rotational springs at the ends are used for the beams. Euler-Bernoulli beams are used for the beams since their shear deformation is not decisive for the overall lateral response. The local stiffness matrix accounts for the flexibility of connections, according to the formulation by Lui and Lopes [29]. By implementing the connection stiffness in the beam element, the columns are modelled as continuous and the beams as discontinuous elements. The cross-sections of the rectangular beams are calibrated such that they have the same stiffness as the composite timber floors in the Woodsol project. In other words, the stiffness of the beams in the planar frame is an equivalent stiffness with respect to Woodsol floor elements. The global stiffness and mass matrices are obtained from static condensation. To account for structural damping, Rayleigh damping is assumed to be equal in all the eigenmodes, calibrated for the lowest and highest eigenfrequency in the system. It is assumed that the connections behave in a linear elastic manner, and thus any nonlinearities for small rotations due to initial slip or other sources are neglected. Therefore, the present study applies for connections with a linear elastic behavior under service load without initial slips. An example of such connections are connections based on axially loaded threaded rods [16,17].

2.2. Wind loading

In this paper, the widely adopted gust factor approach by Davenport [36] and the generalized wind load method outlined in Kareem [37] are used to estimate the wind load. The gust factor approach is a simplified frequency-domain method, in which the standard deviation of the wind load and the dynamic response is multiplied with a peak factor to obtain the peak response. The generalized wind load method used in this paper generates correlated time-series of wind loads on the semi-rigid timber frame structures, based on a Kaimal spectrum [35] and a modal aerodynamic admittance function. A yearly return period and terrain category III is used to assess the serviceability of the response accelerations and displacements.

2.2.1. Gust factor approach

The gust factor approach approximates the peak displacement response with the following expression:

$$x_p = \bar{x} + k_p \sigma_x, \tag{1}$$

where x_p is the peak response, $\bar{x}$ is the mean of the response, k_p is the peak factor, and σ_x is the standard deviation of the response. The standard deviation of the response is approximated by using the following simplified frequency-domain approximation:

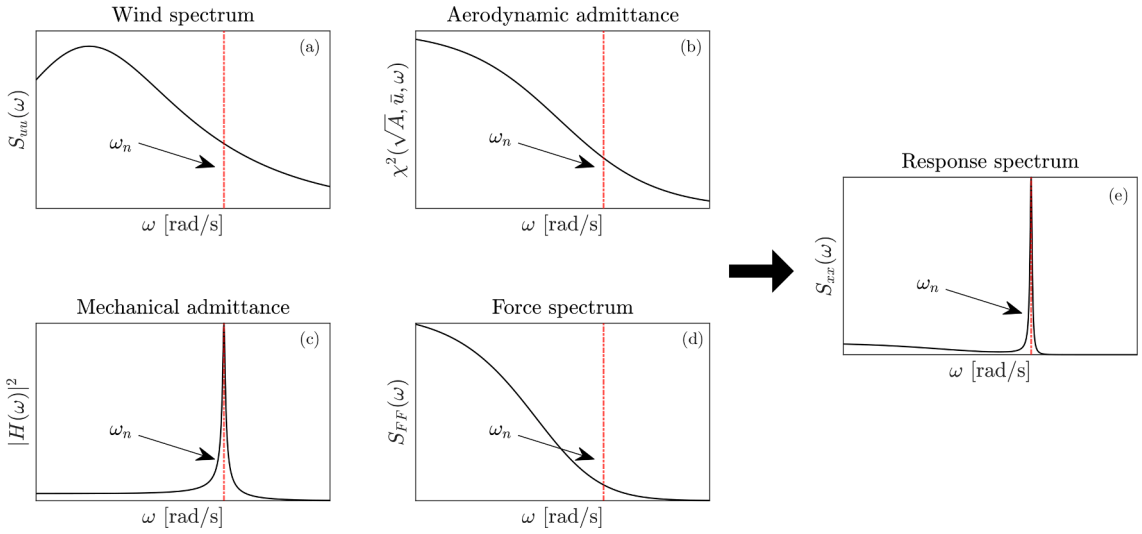

Fig. 2. Frequency-domain spectral response analysis.

$$\frac{\sigma_x^2}{\bar{x}^2} = 4\frac{\sigma_u^2}{\bar{u}^2}[A_B + A_R] = 4\frac{\sigma_u^2}{\bar{u}^2}\left[\int_0^\infty \frac{S_{uu}(\omega)}{\sigma_u^2}\chi^2(\omega)d\omega + \frac{\pi^2}{2\delta}\frac{\omega_n S_{uu}(\omega_n)}{\sigma_u^2}\chi^2(\omega_n)\right], \tag{2}$$

where σ_u^2 is the variance of the wind speed, $\bar{u}$ is the mean wind speed, A_B is the background factor and A_R is the resonant response factor. In the background factor A_B, S_{uu} is the Kaimal spectrum, χ^2 is the aerodynamic admittance function, and ω is the angular frequency of the wind. In the resonant response factor A_R, δ is the logarithmic decrement, and ω_n is the angular fundamental eigenfrequency of the structure. Equation (2) can be analytically derived from the spectral analysis of wind loads on a structure. By substituting Equation (2) into Equation (1) and rearranging, the peak response can be expressed as:

$$\frac{x_p}{\bar{x}} = 1 + 2k_p\frac{\sigma_u}{\bar{u}}\sqrt{B^2 + R^2}, \tag{3}$$

where R^2 approximates the resonant response factor A_R.

For the peak wind velocity, a similar expression is used:

$$u_p = \left(1 + 2k_v\frac{\sigma_u}{\bar{u}}\sqrt{P_0}\right)\bar{u} = c_e\bar{u}, \tag{4}$$

where k_v is the peak velocity factor, P_0 is a nondimensional quantity, and c_e is the exposure factor. Calibrations have shown that the factor $2k_v\sqrt{P_0}$ inherits the approximate value of 7.

To compute the peak static displacement, a structural factor $c_s c_d$ is introduced. The structural factor $c_s c_d$ can be factorized into a size component c_s and a dynamic component c_d. The size component c_s reduces the load due to the lack of coherence of wind pressures on a surface due to turbulence and can be regarded as a rigid or static component. The dynamic or flexible component c_d increases the load due to resonance between the structure and turbulence. The size factor is the ratio between the background response in Equation (3) and the exposure factor in Equation (4). The dynamic factor is the ratio between $x_p/\bar{x}$ in Equation (3) with and without the resonant component. Thus, the structural factor becomes:

$$c_s c_d = \frac{1 + 2k_p\frac{\sigma_u}{\bar{u}}\sqrt{B^2 + R^2}}{1 + 7\frac{\sigma_u}{\bar{u}}} = \frac{1 + 2k_p\frac{\sigma_u}{\bar{u}}\sqrt{B^2}}{1 + 2k_v\frac{\sigma_u}{\bar{u}}\sqrt{P_0}} \cdot \frac{1 + 2k_p\frac{\sigma_u}{\bar{u}}\sqrt{B^2 + R^2}}{1 + 2k_p\frac{\sigma_u}{\bar{u}}\sqrt{B^2}}. \tag{5}$$

The peak wind load can be expressed as:

$$F_p = c_s c_d \cdot c_f q_p A_{\text{ref}}, \tag{6}$$

where c_f is a drag or force coefficient, $q_p = \frac{1}{2}\rho_a u_p^2$ is the peak velocity pressure, and A_{ref} is the windward reference area of the structure. From random vibrations theory, the peak factor can be expressed as:

$$k_p = \sqrt{2\ln(\nu T)} + \frac{0.6}{\sqrt{2\ln(\nu T)}} \approx \sqrt{1.175 + 2\ln(\nu T)}, \tag{7}$$

where ν is the up-crossing frequency, and T is the observation period. The observation period T in this paper is 10 minutes, or 600 seconds. The up-crossing frequency can be derived as:

$$\nu = f_n\sqrt{\frac{R^2}{B^2 + R^2}}, \tag{8}$$

where f_n is the fundamental eigenfrequency of the structure. From the peak wind load F_p, the equivalent peak static displacement can be computed. From random vibrations theory, the variance of the acceleration $\sigma_{\ddot{x}}^2$ can be expressed as:

$$\sigma_{\ddot{x}}^2 = \omega^4\sigma_x^2. \tag{9}$$

By substituting Equation (2) into Equation (9) and neglecting the background response, the variance of the response acceleration can be expressed as:

$$\sigma_{\ddot{x}}^2 = 4\frac{\sigma_u^2}{\bar{u}^2}\frac{\pi^2}{2\delta}\frac{\omega_n S_{uu}(\omega_n)}{\sigma_u^2}\chi^2(\omega_n)\omega^4. \tag{10}$$

If Equation (10) is rearranged, then the final expression for the variance of the response acceleration can be expressed as:

$$\sigma_{\ddot{x}}^2 = (\rho_a C_D \bar{u}\sigma_u A)^2\frac{\pi^2}{2\delta}\frac{\omega_n S_{uu}(\omega_n)}{m^2}\chi^2(\omega_n) \tag{11}$$

In this paper, only the dynamic response is evaluated. Thus, the static component in the structural factor inherits a unit value in Equation (5). In Equation (4), the mean component in the exposure factor is neglected.

Fig. 2 shows the wind-loading model used in the gust factor approach. The gust factor approach is based on spectral analysis, where the response spectrum is approximated. In the gust factor approach, the background factor approximates the steady-state response of the structure. In Fig. 2 the steady-state response is the part of the curve without the peak around the fundamental eigenfrequency. The resonant response factor approximates the peak in the response spectrum. Thus, the gust factor approach is a simplification of the spectral analysis. Due to the simplifications, some accuracy is also lost.

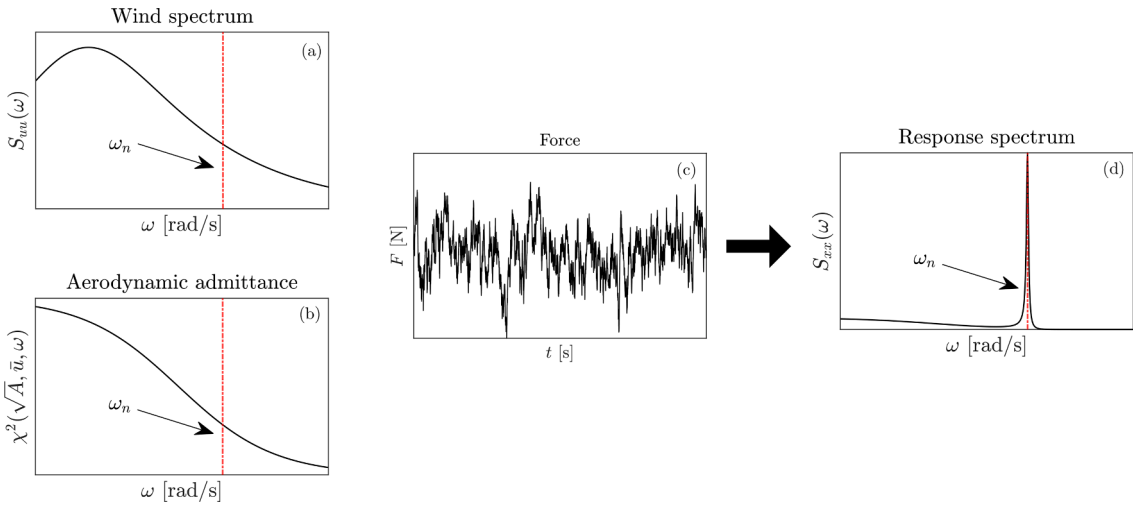

Fig. 3. Time-domain wind spectrum-based response analysis.

2.2.2. *Generalized wind load*

Based on spectral modal analysis, the force spectrum of the generalized wind load can be expressed as:

$$S_{F_k F_l,i}(\omega) = \rho_a^2 \int_A \int_A \phi_{i,k}\phi_{i,l} C_{D,k} C_{D,l} \bar{u}_k \bar{u}_l \mathrm{coh}_{u_k u_l} \sqrt{S_{u_k}(\omega) S_{u_l}(\omega)}\, dA_k dA_l, \tag{12}$$

where ϕ is the mode shape, C_D is the drag or force coefficient, $\bar{u}$ is the mean wind velocity, coh is an exponential coherence function, and dA is an infinitesimal area. $S_{u_{k,l}}(\omega)$ is the Kaimal spectrum adopted by EN1991-1-4 [28]. The indices k and l indicate the spatial coordinate and index i the mode number. Equation (12) can be rewritten as:

$$S_{F_k F_l,i}(\omega) = \left(\rho_a C_{D,r} \bar{u}_r A\right)^2 \sqrt{S_{u_k}(\omega) S_{u_l}(\omega)}\, \chi^2_{\phi_i}(\omega), \tag{13}$$

where $\chi^2_{\phi_i}(\omega)$ is the modal aerodynamic admittance function:

$$\chi^2_{\phi_i}(\omega) = \frac{1}{A^2} \int_A \int_A \frac{C_{D,k} C_{D,l}}{C^2_{D,r}} \frac{\bar{u}_k \bar{u}_l}{\bar{u}^2_r} \phi_{i,k}\phi_{i,l} \mathrm{coh}_{v_k v_l} dA_k dA_l. \tag{14}$$

A full derivation of Equation (12), (13), and (14) can be found Cao [38].

In this paper, correlated time-series of the wind force are generated from Equation (12). The time-series are generated by using the spectral representation method proposed by Shinozuka and Deodatis [39]:

$$x(t_n) = \mathscr{R}e\left\{\frac{1}{N}\sum_{k=0}^{N-1} \sqrt{2\Delta\omega \mathbf{S_{xxk}}}\, e^{i\phi_k} e^{e^{i\omega_k n}}\right\}, \tag{15}$$

where $\Delta\omega S_k$ is the smoothed force spectrum of Equation (13), ϕ_k is a random phase angle, ω_k is an angular frequency, t_n is the time coordinate, x is the generated point, and N is the number of sampling points in the frequency domain.

By using the spectral representation, a time-series of the wind force can be generated, and the dynamic response of the structure can be solved through numerical integration of the modal equation of motion. To compare the peak accelerations and displacements of the generalized wind load with the gust factor approach, the following expressions are used:

$$x_p = 2k_v \sqrt{P_0} \cdot \sigma_x = 7\sigma_x, \tag{16}$$

$$\ddot{x}_{0.95,GWL} = 1.64 \cdot \sigma_{\ddot{x}}. \tag{17}$$

Fig. 3 shows the mixed wind-loading model used for the generalized wind load in this paper. The wind is described in terms of a frequency-domain wind spectrum. From the wind spectrum, a time series, which will inherit the statistical properties of the spectrum, can be generated.

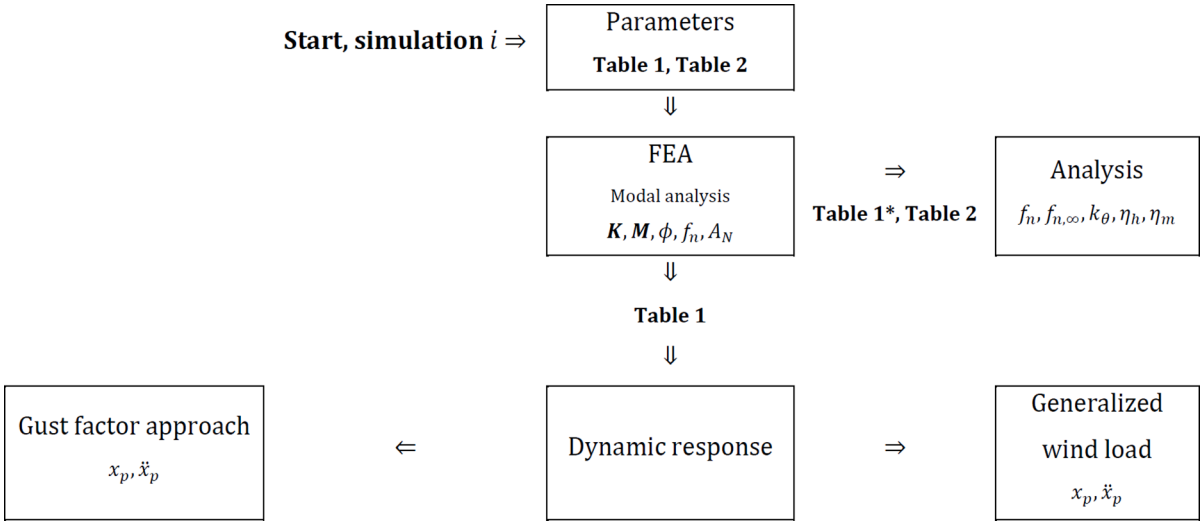

Fig. 4. Flowchart of the method in this paper.

Table 1
Overview of the parameters in the simulations. The elastic modulus E_0 is 13000 MPa and the shear modulus G is 650 MPa for GL30c [40]. *Parameters used to derive the frequency reduction factor.

Floors	Bays	Column height b_c = 0.28 m	Beam height b_b = 0.28 m	Beam-to-column stiffness	Translational support stiffness		Rotational support stiffness	Beam length	Floor height	Surface load	Line load	Wind velocity
n_{floor}	n_{bay}	h_c	h_b	k_θ	$k_{x,sup}$	$k_{z,sup}$	$k_{\theta,sup}$	L_b	H	p_S	p_L	$v_{b,0}$
–	–	M	m	Nm/rad	N/m	N/m	Nm/rad	m	m	N/m^2	kg/m	m/s
5*	2	0.30*	0.625	10×10^6	10^7		1*	6*	3.0*	1600	391	22
	3	0.38*	0.725	15×10^6	10^8		5×10^6*	8*	3.5*	2600	611	26
	4	0.46*	0.825	20×10^6	10^9*		10×10^6	10*	4.0*	3000*	734*	30
				$10^3 - 10^{11}$*			10^{12}*			5000	1223	
6	2	0.30		10×10^6						7000	1468	22
	3	0.38		15×10^6							1713	26
	4	0.46		20×10^6								30
				10×10^6								
7*	2	0.30*, 0.38*		15×10^6								22
	3	0.46*, 0.54		20×10^6								26
	4			$10^3 - 10^{11}$*								30
8	2	0.38, 0.46		10×10^6								22
	3	0.54, 0.62		15×10^6								26
	4			20×10^6								30
				10×10^6								
9*	2	0.46*, 0.54*		15×10^6								22
	3	0.62*, 0.70		20×10^6								26
	4			$10^3 - 10^{11}$*								30
10	2	0.54, 0.62		15×10^6								22
	3	0.70, 0.78		20×10^6								26
	4			25×10^6								30

To obtain the force spectrum, the wind spectrum and the aerodynamic admittance are multiplied. From the force time-series, the response can be computed by solving the equation of motion numerically. However, the mixed wind-loading model is computationally expensive due to the need to generate time series and the numerical solution of the equation of motion.

2.3. Mass distribution

The effect of mass and mass distribution is assessed in terms of a mass factor η_m, height factor η_h, and a normalized acceleration $A_{N,m}$. The mass factor η_m is normalized with respect to the lightest case, the height factor η_h is the height of an added mass h_m normalized with respect to adding the mass at the top-floor of the structure h, and the normalized acceleration for the mass factor $A_{N,m}$ is the top floor acceleration of the frame normalized with respect to a mass factor η_m and height factor η_h of 1.0:

$$\eta_m = \frac{p_S}{1600\,\frac{\mathrm{N}}{\mathrm{m}^2}}, \eta_h = \frac{h_m}{h}, A_{N,m} = \frac{\ddot{x}(\eta_m, \eta_h)}{\ddot{x}(\eta_m = 1, \eta_h = 1)}. \tag{18}$$

2.4. Overview of simulations

The serviceability limit state is assessed in terms of peak accelerations and displacements. Focus is given on the accelerations. The requirements by ISO10137 [26] are applicable for the annual acceleration and a probability factor c_{prob} of 0.73. Terrain category III was used for the simulations.

The method of analysis is summarized in Fig. 4. For each unique frame with a set of parameters, an FE analysis is carried out to compute the stiffness matrix **K**, the mass matrix **M**, the mode shapes ϕ, and the natural eigenfrequencies of the frame f_n. Both the gust factor approach and the generalized wind load are applied. For the generalized wind load, the computations are repeated five times for each combination to account for the stochastic behavior of the generated wind loads. The main output parameters of the simulations are the top-floor accelerations and displacements.

Before performing the complete set of simulations, an initial parameter study or a sensitivity analysis, was performed to investigate the significance of different parameters. To perform the parameter study, a reference frame is defined with ten floors $n_{\mathrm{floor}} = 10$, floor height$H = 3$ m, number of bays $n_{\mathrm{bay}} = 2$, bay length$L_b = 8$ m, connection stiffness $k_\theta = 20\,000$ kNm/rad, beam dimensions $h_b \times b_b = 0.825\,\mathrm{m} \times 0.28$ m, column dimensions $h_c \times b_c = 0.62\,\mathrm{m} \times 0.28$ m, translational support stiffness $k_{x,z} = 10^{12}$ N/m (rigid supports), $k_{\theta,\mathrm{sup}} = 1$ N/m (pinned supports), damping ratio $\xi = 0.02$, windward building width $b = 24$ m, frame spacing $s = 2.4$ m, and surface floor load $p_s = 2.6$ kN/m^2. From the reference frame, each of the parameters are varied individually to quantify their effect on the top floor accelerations and

Table 2
Overview of the parameters in the analysis of the effect of the location and amount of added mass in one floor.

Floors	Bays	Column height b_c = 0.28 m	Beam height b_b = 0.28 m	Beam-to-column stiffness	Translational support stiffness		Rotational support stiffness	Beam length	Floor height	Surface load	Line load	Mass factor	Height factor
n_{floor}	n_{bay}	h_c	h_b	k_θ	$k_{x,sup}$	$k_{z,sup}$	$k_{\theta,sup}$	L_b	H	p_S	p_L	η_m	η_h
–	–	m	m	Nm/rad	N/m	N/m	Nm/rad	M	m	N/m^2	kg/m	–	–
10	2	0.62	0.625	15×10^6	10^9		1	6	3.0	1600	391	1, 2	0.3, 0.4
	3	0.70	0.725	20×10^6			10×10^6	8	4.0			3, 4	0.5, 0.6
	4	0.78	0.825	25×10^6				10				5	0.7, 0.8
	5												0.9, 1.0

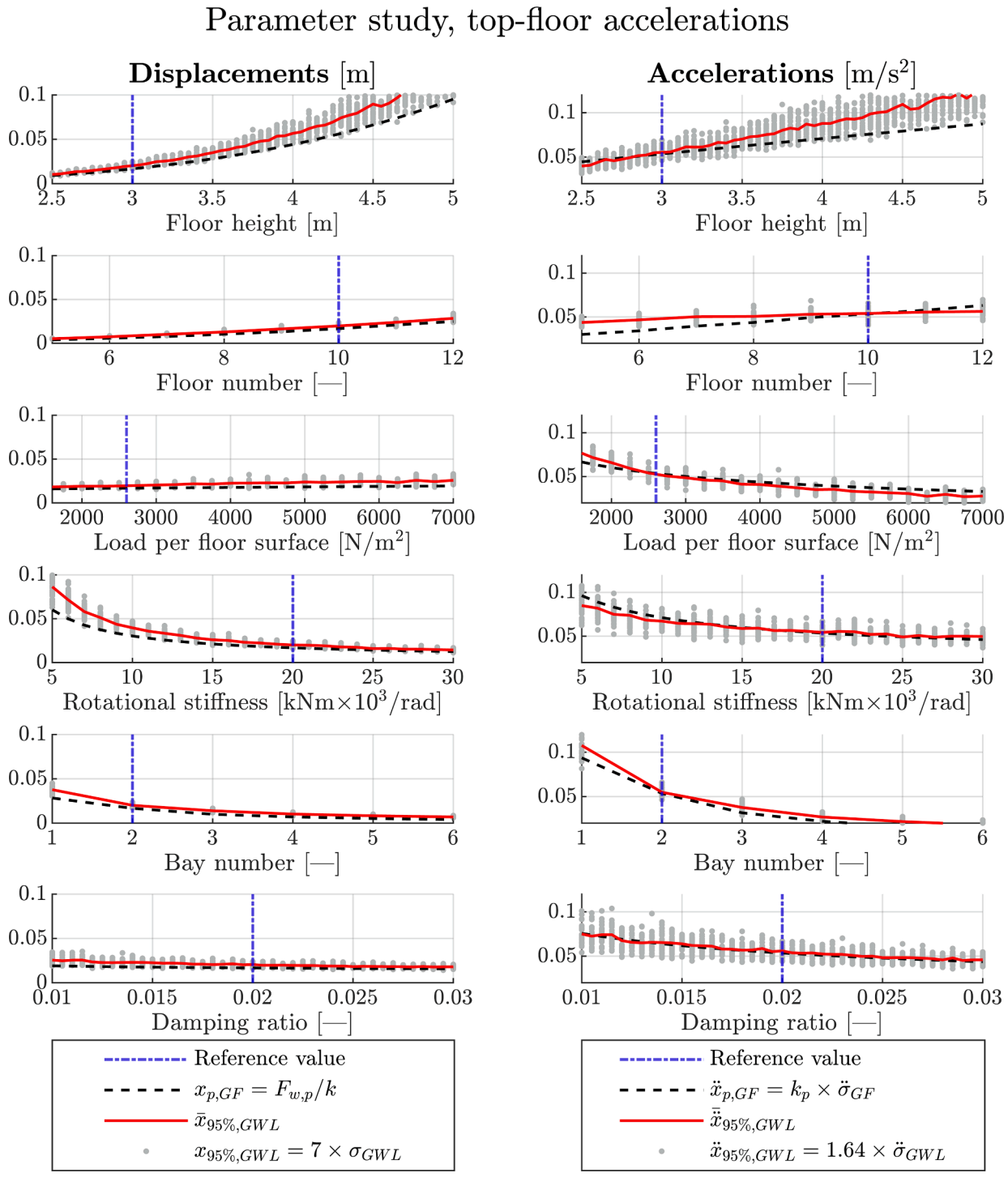

Fig. 5. Displacements and accelerations for the gust factor approach (black dashed line) and generalized wind loading (dots). The simulations are for the reference frame with varying one parameter at a time. The reference value for the parameter is shown with the blue solid line. (For interpretation of the references to colour in this figure legend, the reader is referred to the web version of this article.)

displacements. The varied parameters are the number of floors, number of bays, beam dimensions, column dimensions, connection stiffness, horizontal support stiffness, vertical support stiffness, rotational support stiffness, damping ratio, beam length, floor height, and vertical surface load. A total of 9540 simulations were performed in the initial parameter study.

The parameters used in the complete set of simulations are summarized in Table 1. These parameters are based on the results from the parameter study. As seen in Table 1, the varied parameters are the number of floors and bays, cross-sectional dimensions of the columns and the beams, rotational stiffness of the connections, translational and rotational stiffness of the supports, floor height and bay length, vertical surface load or the mass on each floor, and the basic wind speed. The parameters which are held constant are the frame spacing $s = 2.4$ m, building width $b = 24$ m, and damping ratio $\xi = 2\%$. This is a common assumption for timber although the damping of timber buildings under service-load is a parameter that is not fully investigated yet. In this paper, a constant damping ratio $\xi = 2\%$ is used, based on Feldmann

Table 3
Qualitative observations of the trends, effects, significance, and flexibility of the different parameters on the displacements and accelerations (flexibility denotes the freedom for the structural engineer to change the values of the parameters based on architectural plans and physical in-situ conditions). The effect is given in positive change (+), and negative change (−) in the values of the accelerations and displacements).

Parameter	Trend, displacements	Trend, accelerations	Displacements		Accelerations		Parameter flexibility
			Effect	Significance	Effect	Significance	
Floor height	Linear	Exponential	+	High	+	High	Low
Floor number	Exponential	Linear	+	High	+	High	Low
Load	Linear	Inverse exponential	+	Low	−	High	Medium
Beam stiffness	Inverse exponential	Inverse exponential	−	Medium	−	Medium	High
Column stiffness	Inverse exponential	Inverse exponential	−	Medium	−	Medium	High
Connection stiffness	Inverse exponential	Inverse exponential	−	High	−	High	High
Rotational support stiffness	Inverse exponential	Linear	−	Medium	−	Low	Medium
Horizontal support stiffness	Inverse exponential	Constant	−	Low	−	None	Low
Vertical support stiffness	Inverse exponential	Inverse exponential	−	Medium	−	Medium	Low
Bay number	Inverse exponential	Inverse exponential	−	High	−	High	Medium
Beam length	Linear	Linear	+	Medium	−	Medium	Medium
Damping ratio	Inverse exponential	Inverse exponential	−	Medium	−	High	Low

et al. [31]. All combinations of the parameters in Table 1 are simulated, resulting in 721 710 unique frames subjected to three different wind loads. In total, 10.8 million simulations were performed.

After analyzing of the frames according to Table 1, a new series of simulations is performed investigating the impact of uniform and non-uniform mass distributions on the peak accelerations. The parameters for these simulations are summarized in Table 2. In these series, a total of 194 400 unique frames were computed, resulting in 972 000 simulations in total.

The number of floors and bays are chosen to be within what is thought to be a reasonable practical range. For frames with more than 10 floors, it is difficult to meet the serviceability criteria for moment-resisting skeleton frames with semi-rigid connections. Columns with typical dimensions and strength class GL30c from EN 14080 [40] were assumed, so that they also satisfy the ultimate limit state. The beam cross sections are equivalent cross sections calibrated from the composite timber slab used in the Woodsol system [15]. The connection and support stiffnesses are based on the connections with threaded rods developed as part of the Woodsol system, where each plane of threaded rods contribute with approximately 4000 to 5000 kNm/rad [15]. To achieve the connection stiffnesses used in this paper, three to six planes of threaded rods are assumed. The translational support stiffness values represent the typical range of soil stiffnesses. The beam length is restricted upwards by human-induced vibrations, and downwards by practical architectural purposes. The floor heights are typical floor heights for buildings. The surface loads represent the mass of slabs and live loads for different slab systems. Due to the large discrepancy between the two numerical methods used in this paper for low masses, additional simulations were performed to investigate this further. The wind velocities are typical for Europe.

3. Results and discussion

3.1. Initial parameter study

The results of the initial parameter study are summarized in Fig. 5. A qualitative description of the observed trends is given in Table 3. In the generalized wind load, each combination of the parameters is simulated 30 times to account for stochastic variability. From this parameter study, the parameters with the highest significance on the top floor displacements are the floor height, the number of floors, rotational stiffness of the connections, and the number of bays. The parameters with the lowest impact on the displacements are the mass in terms of load per unit floor surface, and the horizontal stiffness of the supports. The parameters with the highest significance on the top floor accelerations are the floor height, number of floors, mass, rotational stiffness of the

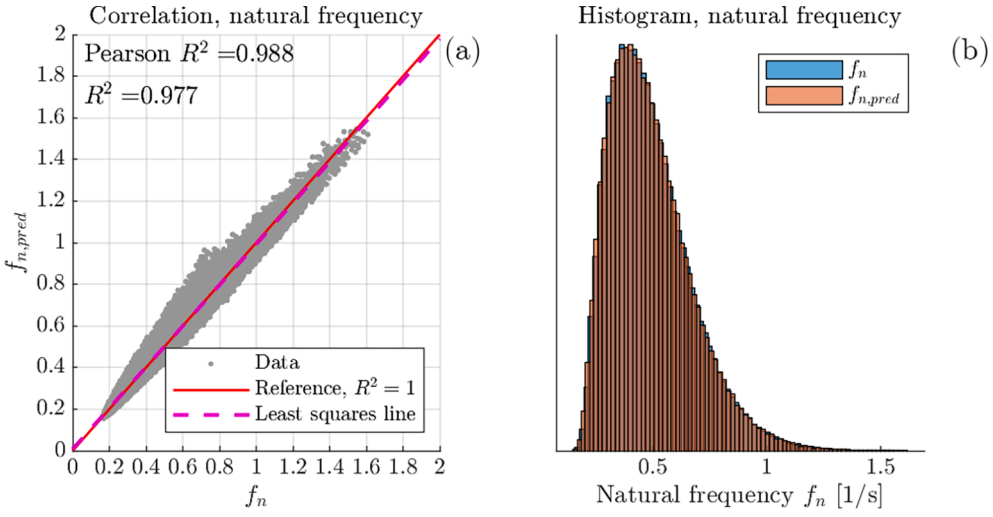

Fig. 6. **(a)** Correlation plot between the fundamental eigenfrequency from the FE database and the predicted fundamental eigenfrequency, and **(b)** histogram of the fundamental eigenfrequency from the FE database and the predicted fundamental eigenfrequency.

connections, number of bays, and the damping ratio. The parameters with the lowest influence on the accelerations are the horizontal and the rotational stiffness of the supports.

3.2. Dynamic properties

3.2.1. Fundamental eigenfrequency

The power peak of turbulent winds for the simulated wind velocities is about 0.03 Hz. Although the fundamental eigenfrequencies f_n of the frames are low, they are still well separated from the power peak of the wind. For some super-tall structures, the fundamental eigenfrequency f_n is in the order of 0.05 Hz [41].

Nonlinear regression on the database is performed by assuming equations of the following form:

$$Y_{\text{pred}} = c \cdot \prod_{\text{i}}^{\text{n}} X_i^{b_i}.$$

For the fundamental eigenfrequency, the regression on the FE database results in the following expression for the prediction of the fundamental eigenfrequency $f_{n,\text{pred}}$:

$$f_{n,\text{pred}} = \frac{c_i}{h^{0.5}} \frac{\left(N_{\text{bay}} \frac{EI_c}{H^3}\right)^{0.22} \left(N_{\text{bay}} k_\theta\right)^{0.21} k_{x,z,\text{sup}}^{0.018}}{\left(N_{\text{floor}} N_{\text{bay}} L_b \times p\right)^{0.5}}, \tag{19}$$

where c_i is a parameter depending on the rotational stiffness of the supports. For pinned supports, the support coefficient c_i is 1.0. For a semi-rigid support stiffness of 5000 kNm/rad, the support coefficient c_i is 1.09. For a semi-rigid support stiffness of 10 000 kNm/rad, the support coefficient c_i is 1.13. The lowest correlations occur for the most flexible frames. In Equation (19), observe that the denominator is the square root of the total mass of the structure. This is in full agreement with the analytical expression for the fundamental eigenfrequency of a single degree of freedom system. If the expression is rearranged, the total height h is the most important parameter as it is directly linked to the flexibility of the structure. According to Equation (19), the column stiffness and the connection stiffness affect the fundamental frequency almost equally, but to a lesser degree compared to the height of the building. The simulated frames show little sensitivity to the translational stiffness of the supports. This may be attributed to the limited rigid body behavior of the columns and a limited ability to transfer shear forces. It is expected that structures with shear walls or structural panels that can transfer shear forces and rotate as rigid bodies are more sensitive to the translational stiffness of the supports.

Fig. 6 shows the correlation plot and histograms for the predicted fundamental eigenfrequency $f_{n,\text{pred}}$ in Equation (19) against the analytical FE database obtained by modal analysis. The histogram of the predicted fundamental eigenfrequency $f_{n,\text{pred}}$ matches the histogram of the analytical fundamental eigenfrequency f_n almost exactly. For the correlation plot, the data points are quite narrowly distributed along the least-squares line. The outliers are the most slender, flexible, and light frames. To evaluate the goodness of fit, the following coefficient of determination R^2 was used:

$$R^2 = 1 - \frac{\sum_i \left(y_i - y_{\text{pred}}\right)^2}{\sum_i \left(y_i - \bar{y}\right)^2} \tag{20}$$

where y_i is the analytical or simulated data, y_{pred} is the value from the regressions, and $\bar{y}$ is the mean value of the analytical or simulated data y_i.

3.2.2. Mode-shape parameter

According to EN1991-1-4 [25] the mode shape of the fundamental mode of vibration is given by:

$$\Phi = \left(\frac{z}{h}\right)^{\zeta}, \tag{21}$$

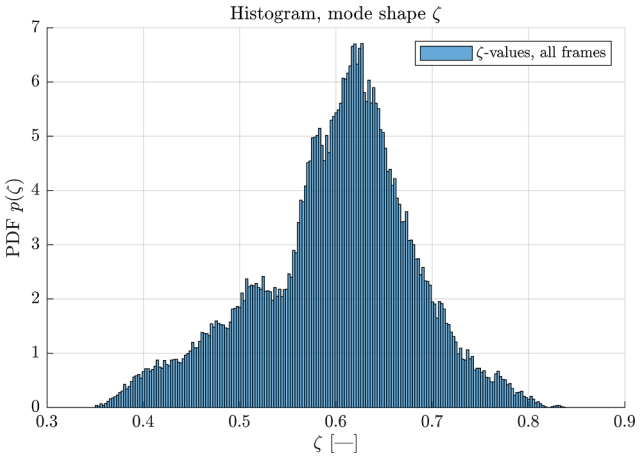

Fig. 7. Histogram for the mode shape parameter of all the simulated frames.

where ζ is a mode-shape parameter ranging from 0.6 for slender structures to 2.5 for stiff structures. A mode-shape parameter $\zeta = 1.0$ is typically suitable for a building with a central core and peripheral columns or larger columns in addition to shear bracings. A value of $\zeta = 0.6$ is typically suitable for a slender structure with no load-sharing walling or cladding. This is in good agreement with the simulated frames. The mode shape parameter is quantified for all frames so that the mode shape according to Equation (21) fits the FE results the best. Fig. 7 shows a histogram for the mode shape parameter ζ of all the simulated frames. The mode shape parameter depends on the stiffness and mass. Observe that the peak is concentrated at a mode shape parameter of about 0.61

It is expected that the histogram in Fig. 7 is non-smooth since the results in the dataset themselves are discrete.

3.2.3. Frequency reduction factor

The effect of the connection stiffness on the fundamental eigenfrequency is investigated by following the flowchart in Fig. 4 for Table 1. From the computations of the fundamental eigenfrequencies, a unique f_n-k_θ sigmoid behavior is observed. To make the sigmoid behavior of each of the frames comparable, the fundamental eigenfrequencies f_n are normalized with respect to the fundamental eigenfrequency of a frame with rotationally rigid connections $f_{n,\infty}$ and pinned supports. The normalized fundamental eigenfrequency $f_n/f_{n,\infty}$ varies from zero to 1.0. For each unique frame, a unique sigmoid is formed. To unify all the sigmoids, an adjusted connection stiffness $k_{\theta,\text{adj}}$ is introduced and can be expressed as:

$$k_{\theta,\text{adj}} = \left(\frac{n_{bay}}{n_{floor}^2} \cdot \frac{L_c^4}{EI_c^6} \cdot \frac{L_b^3}{EI_b}\right)^{\frac{1}{10}} \cdot k_\theta. \tag{22}$$

Based on the adjusted rotational stiffness of connections $k_{\theta,\text{adj}}$ in Equation (22), a unified sigmoid relationship between the normalized fundamental eigenfrequency $f_n/f_{n,\infty}$ and the adjusted connection stiffness can be observed. Based on this observation, the following sigmoid is proposed:

Table 4
Overview of the rigidity index k_s according to the support conditions.

Support condition	Rigidity index k_s
Pinned ($k_{\theta,\text{sup}} = 0$)	0
Semi-rigid ($k_{\theta,\text{sup}} = 5000$ kNm/rad)	2
Rigid ($k_{\theta,\text{sup}} = \infty$)	5

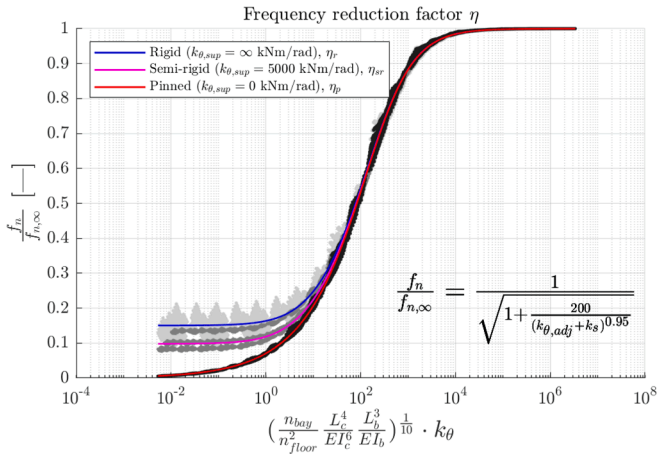

Fig. 8. The frequency reduction factor η with respect to the adjusted connection stiffness $k_{\theta,\mathbf{adj}}$. The three different lines are for different support conditions, whereas the x-axis represents the connection stiffnesses in the frames.

$$\frac{f_n}{f_{n,\infty}} = \eta = \frac{1}{\left(1 + \frac{200}{\left(k_{\theta,\mathrm{adj}} + k_s\right)^{0.95}}\right)^{0.5}}, \tag{23}$$

where k_s is a support rigidity index. Equation (23) is named the frequency reduction factor. The support rigidity index k_s adjusts the sigmoid, or the frequency reduction factor η, according to the type of support conditions on the foundations. The support rigidity index k_s has a range from zero (for pinned supports), to five (for rotationally rigid supports). Table 4 provides an overview of the values of the rigidity index.

By rearranging Equation. (23), the following expression is obtained:

$$f_n = \frac{1}{\sqrt{1 + \frac{200}{\left(k_{\theta,\mathrm{adj}} + k_s\right)^{0.95}}}} \cdot f_{n,\infty}. \tag{24}$$

The implication of this simple yet accurate expression for the fundamental eigenfrequency, is a simple equation to determine the fundamental eigenfrequency of a semi-rigid frame f_n from the fundamental eigenfrequency $f_{n,\infty}$ of a frame with rotationally rigid beam-to-column connections. In Fig. 8, the frequency reduction factor η for different support conditions is plotted together with theoretical values. The black dots indicate the data for pinned supports, the dark grey dots indicate the data for semi-rigid supports with a support stiffness $k_{\theta,\mathrm{sup}}$ of 5000 kNm/rad, and the light grey dots indicate the data for rigid supports. Observe that the normalized fundamental eigenfrequency $f_n/f_{n,\infty}$ converges to zero when the adjusted connection stiffness is very low $k_{\theta,\mathrm{adj}}$ for pinned supports. When the adjusted connection stiffness $k_{\theta,\mathrm{adj}}$ is very high, the normalized fundamental eigenfrequency $f_n/f_{n,\infty}$ converges towards 1.0. The frequency reduction factor η follows the sigmoid shape of the frames with great precision. The behavior is in agreement with the observations by Lui and Lopes [29].

For the semi-rigid and rigid supports, observe that the normalized fundamental eigenfrequency $f_n/f_{n,\infty}$ or the frequency reduction factor for semi-rigid supports η_{sr} and rigid supports η_r does not converge towards zero as for pinned supports. For the rigid support, the frequency reduction factor η_r converges towards a value of about 0.15. For the semi-rigid support, the frequency reduction factor η_{sr} converges towards a value of about 0.1. Both the semi-rigid η_{sr} and the rigid supports η_r converge to the same curve as the pinned supports with an increasing adjusted connection stiffness $k_{\theta,\mathrm{adj}}$. The rotational support conditions are not of high importance for the fundamental eigenfrequency of the frames during serviceability. The adjusted connection stiffness $k_{\theta,\mathrm{adj}}$ is above 10^2 for most engineering structures, yielding a frequency reduction factor η of about 0.5.

3.3. Structural response

3.3.1. Accelerations

Fig. 9 shows a correlation plot and histograms of the percent bias between the response accelerations determined by the gust factor (GF) approach and the generalized wind load (GWL). From the correlation plot, the gust factor approach results in overall lower accelerations than the generalized wind load with an R^2 of 0.81. From the histograms, the deviations between the gust factor approach and the generalized wind load are larger for the lightest frames than the heavier frames. Except for a surface load p_S of 7000 N/m^2, the other surface loads p_S result in a median in which the gust factor approach gives lower accelerations. In general, for heavier frames a better agreement is observed between the gust factor approach and the generalized wind loading methods. The gust factor approach underestimates the results significantly compared with the generalized wind loading for lighter frames. For the lightest frames, a median percent bias of up to 50% is observed. From this, the gust factor approach is nonconservative with respect to accelerations for light frames compared with the generalized wind load.

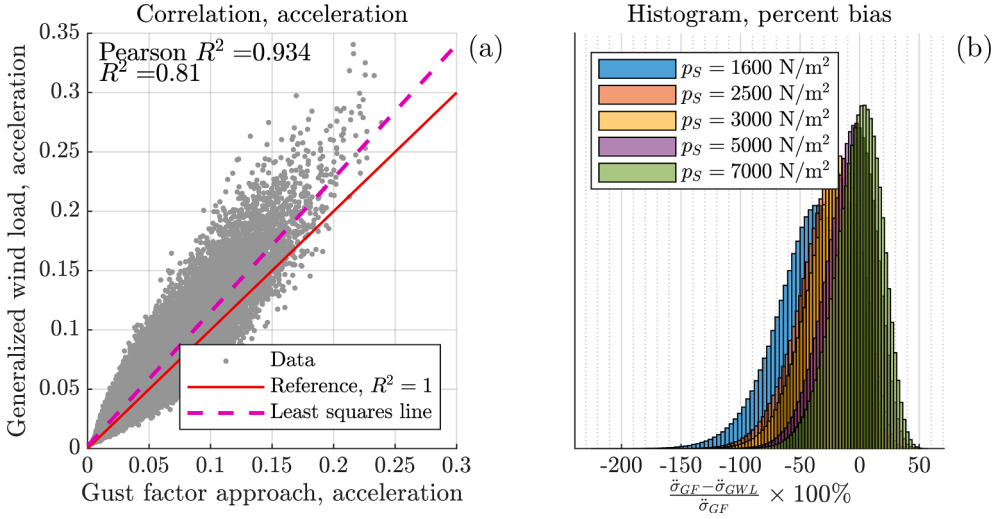

Fig. 9. (a) Correlation plot between the response accelerations determined by the gust factor approach and the generalized wind load, and **(b)** histograms of the percent bias between response accelerations of the gust factor approach and the generalized wind load for different surface loads.

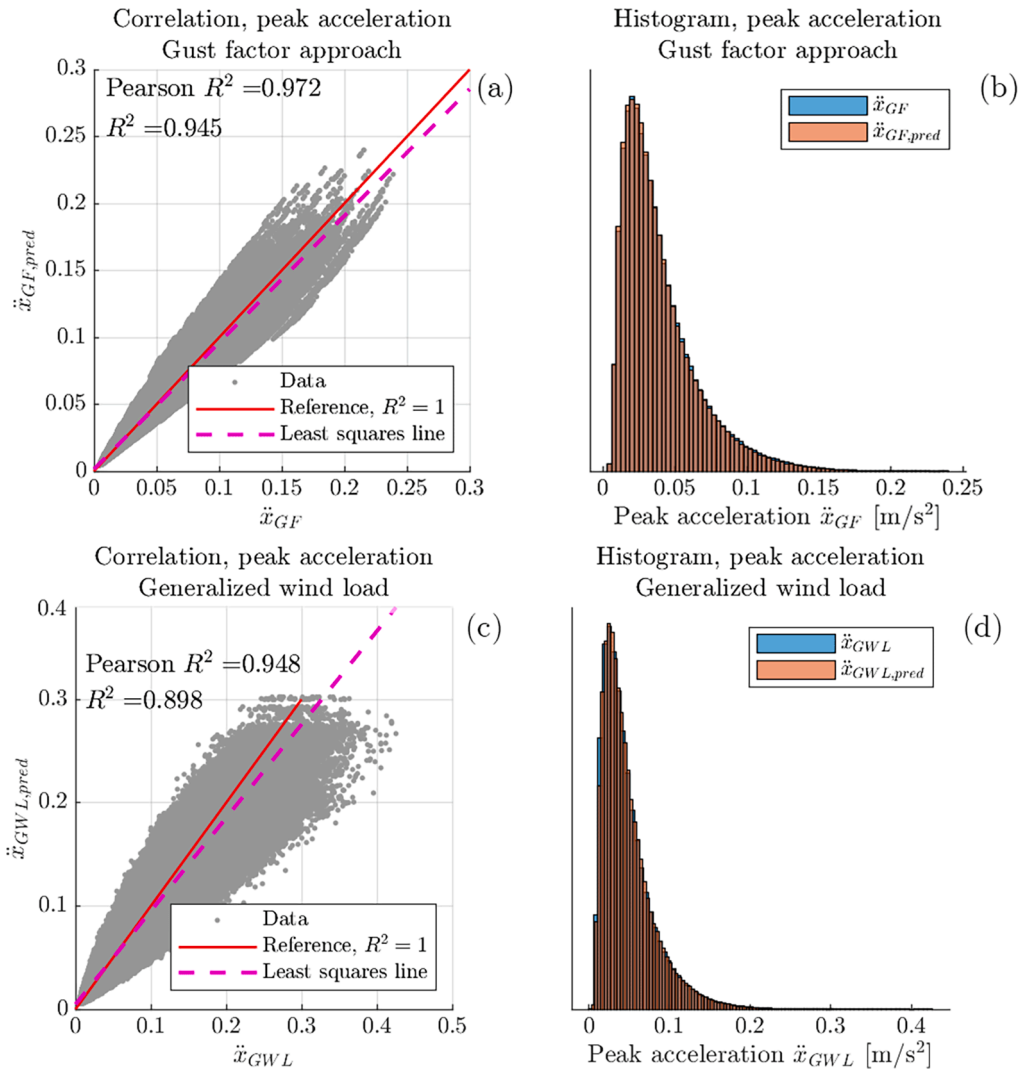

Fig. 10. Correlation plots and histograms for the regression of the predicted peak response accelerations $\ddot{x}_{pred}$ for the **(a)** and **(b)** gust factor approach, and the **(c)** and **(d)** generalized wind load.

Based on the results in Table 3, the acceleration should be a function of the geometry, load, stiffness, and damping ratio. In this paper, a damping ratio of 2% is chosen for the simulations. By use of nonlinear regression, the resulting expressions for the peak response accelerations for the gust factor approach and the generalized wind load are obtained:

$$\ddot{x}_{GF,\text{pred}} = \frac{\rho_a c_f b \overline{u}}{N_{\text{floor}} N_{\text{bay}} L_b \times p} \frac{1}{2\pi\xi} \overline{u}^{1.4} S_L^{1.2} f_n^{-0.44}, \tag{25a}$$

$$\ddot{x}_{GWL,\text{pred}} = \frac{\rho_a c_f b \overline{u}}{N_{\text{floor}} N_{\text{bay}} L_b \times p} \frac{1}{2\pi\xi} \overline{u}^{1.1} S_L^{0.75} f_n^{-0.34}. \tag{25b}$$

where S_L is the normalized Kaimal spectrum in EN1991-1-4 [25]. For the generalized wind load in Equation (25b), the predicted peak acceleration is assumed as the 95% percentile for a Gaussian distribution. Observe that the exponents of the normalized wind spectrum and the fundamental eigenfrequency are quite similar in both expressions in Equation (25) It is assumed that the damping ratio plays an important role for the accelerations, as suggested by the results of the initial parametric study in Fig. 5. However, the damping ratio is not parametrized in this paper.

Fig. 10 shows the correlation plots and histograms for the predicted peak response accelerations $\ddot{x}_{\text{pred}}$ in Equation (25) against the analytical expression for the gust factor approach, and the stochastic simulations for the generalized wind load. In both cases, the histogram of the predicted peak acceleration $\ddot{x}_{\text{peak}}$ matches the analytical expression and the stochastic simulations very well. In the correlation plots, the gust factor approach has a narrower spread and a more gradual tail for the higher accelerations than the generalized wind load. This observation may be explained by the stochastic nature of the calculated response based on the generalized wind loading method. It can be seen in the histograms and the correlation plots that the accelerations in the gust factor approach are lower than in the generalized wind load.

Like the expression of the predicted fundamental eigenfrequency in Equation (19), the outliers are the lightest and most flexible frames.

ISO10137 [26] defines serviceability criteria for wind-induced vibrations in structures. They are based upon subjective comfort criteria and gives the acceleration criteria with respect to the fundamental eigenfrequency of the considered structure. Fig. 11 shows the peak response accelerations for the gust factor approach and the generalized wind load for different wind velocities in the form of intensity maps. Darker colors indicate higher concentrations of simulated frames. The more even distribution for the generalized wind load can be attributed to stochastic variations in the generated time-series and response accelerations.

For a basic wind velocity $v_{b,0}$ of 22m/s, all frames in the generalized wind load satisfy the serviceability criteria for both office and residential structures. In the gust factor approach, the majority of the frames satisfy the serviceability criteria. For the higher wind velocities $v_{b,0}$, the cloud

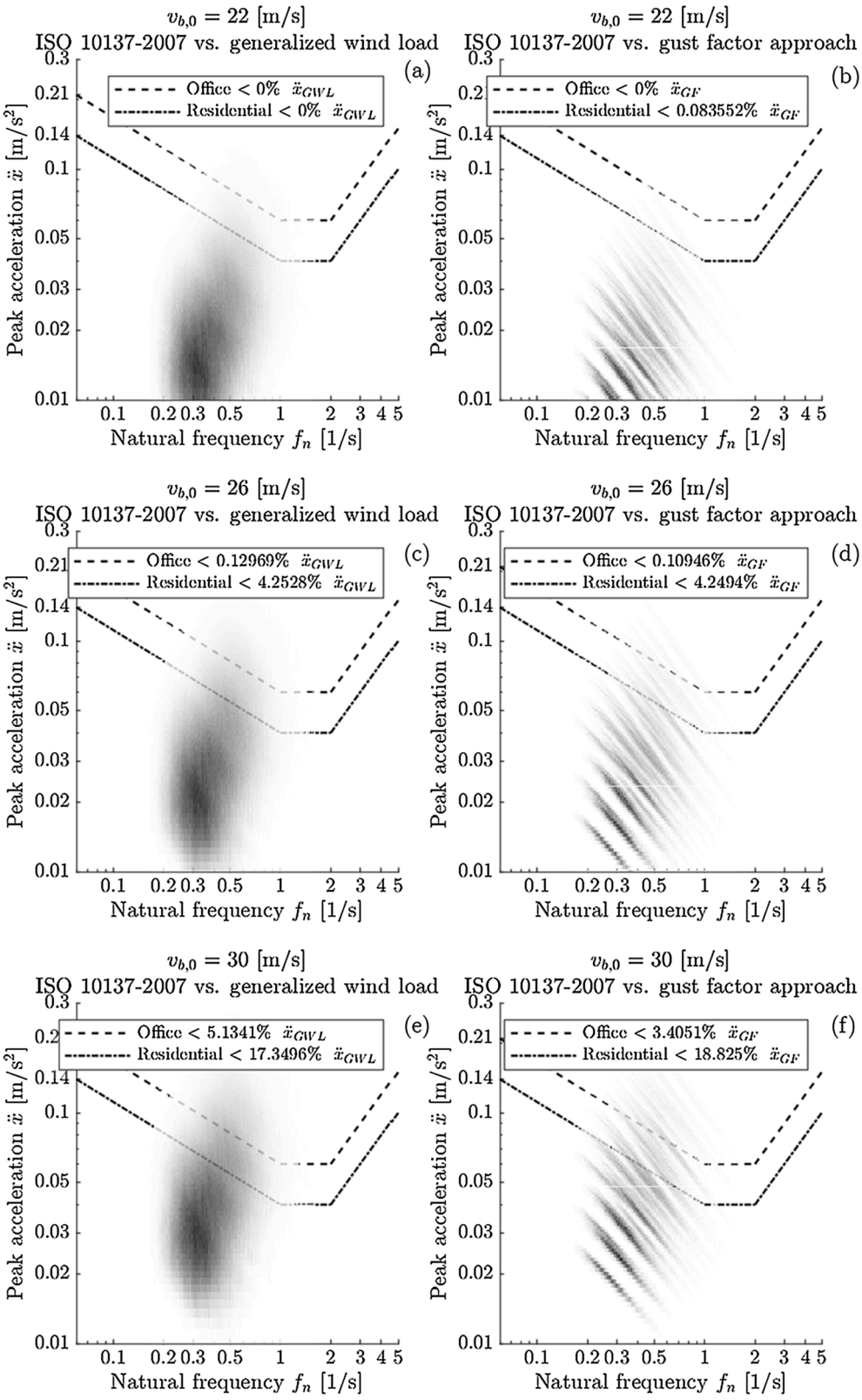

Fig. 11. Peak acceleration compared to criteria for wind-induced vibrations according to ISO10137 [26] and intensity maps of the peak accelerations for the gust factor approach and the generalized wind load for different wind velocities.

of peak accelerations moves upwards with more frames not satisfying the serviceability criteria. However, most of the frames do satisfy the strictest serviceability criteria of residential structures for all the wind velocities $v_{b,0}$. The intensity maps in Fig. 11 show that the wide range of semi-rigid timber frames simulated in this paper are feasible. The frames that do not satisfy the serviceability criteria are the lightest and most flexible ones.

Table 5
Key metrics of the regression of the peak displacement for the gust factor approach and the generalized wind load.

				Pinned	Semi-rigid	Semi-rigid
Support stiffness		$k_{\theta,\text{sup}}$	Nm/rad	1	5×10^6	10×10^6
Support coefficient	Gust factor approach	c_i	–	1.00	0.843	0.791
	Generalized wind load				0.801	0.736

3.3.2. Displacements

In this paper, only the structural response to the turbulent component of the wind loads is simulated. Moreover, the return period of the wind loading is one year, which is used to control wind-induced accelerations. The serviceability checks for displacements or horizontal sway and inter-story drifts are usually performed for the frequent and characteristic serviceability load combinations according to EN 1990 [42], or in other words for a higher return period than one year. Thus, the response displacements are of little interest and are only used for model verification. Based on nonlinear regression on the FE results, the resulting expressions for the peak displacements are:

$$x_{GF} = c_i \frac{\frac{1}{2}\rho_a \overline{u}^2 c_f \left(N_{\text{floor}} Hb\right)\left(\frac{L_u}{\sqrt{N_{\text{floor}} Hb}}\right)^{5.34}}{N_{\text{bay}}^{1.25}\left(\frac{EI_b}{L_b^3}\right)^{0.05}\left(\frac{EI_c}{H^3}\right)^{0.4} k_\theta^{0.7} k_{x,z,\text{sup}}^{0.06}}, \tag{26a}$$

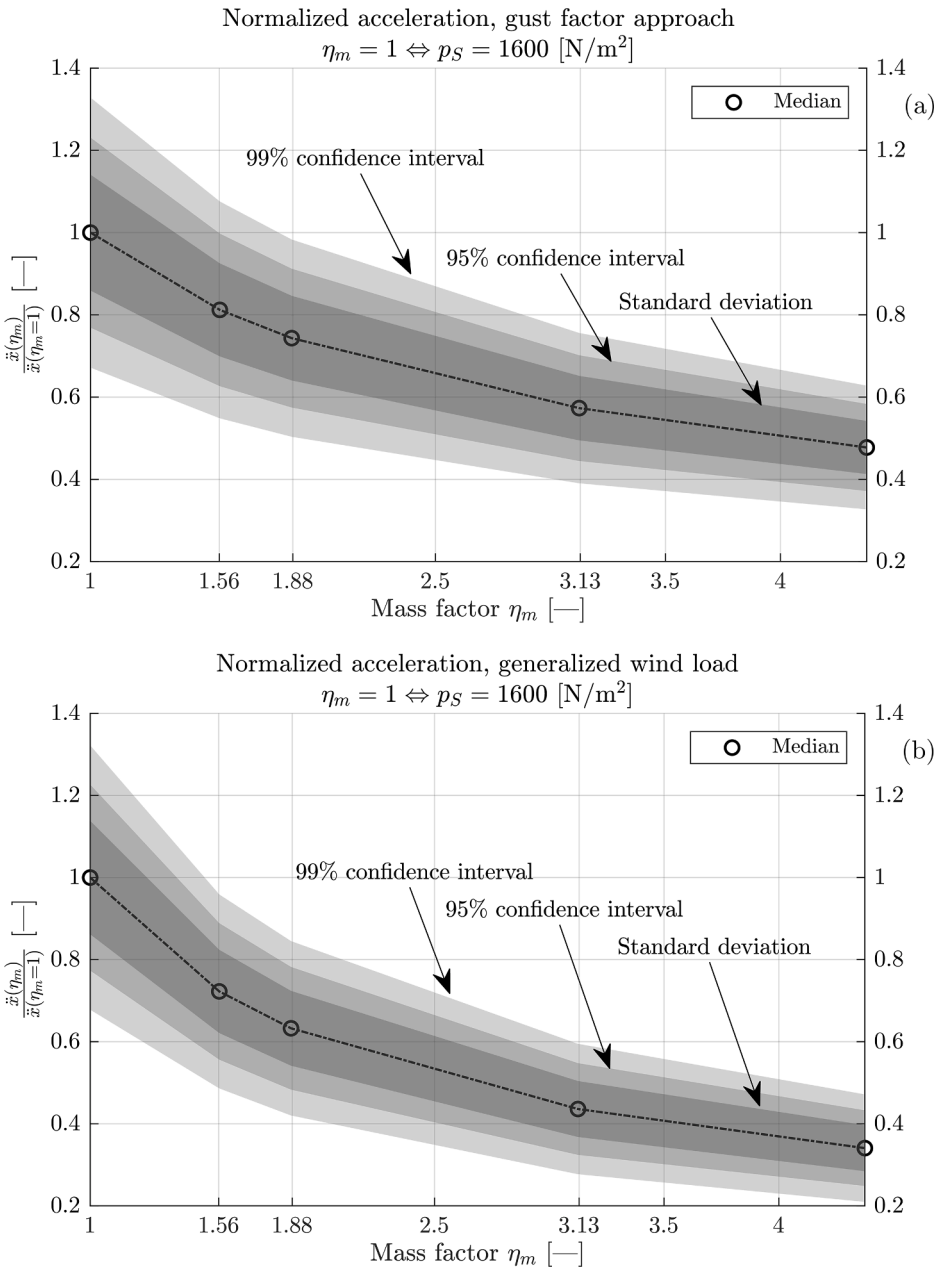

Fig. 12. Normalized acceleration $A_{N,m}$ with respect to the mass factor η_m for a uniform mass distribution for **(a)** the gust factor approach, and **(b)** the generalized wind load.

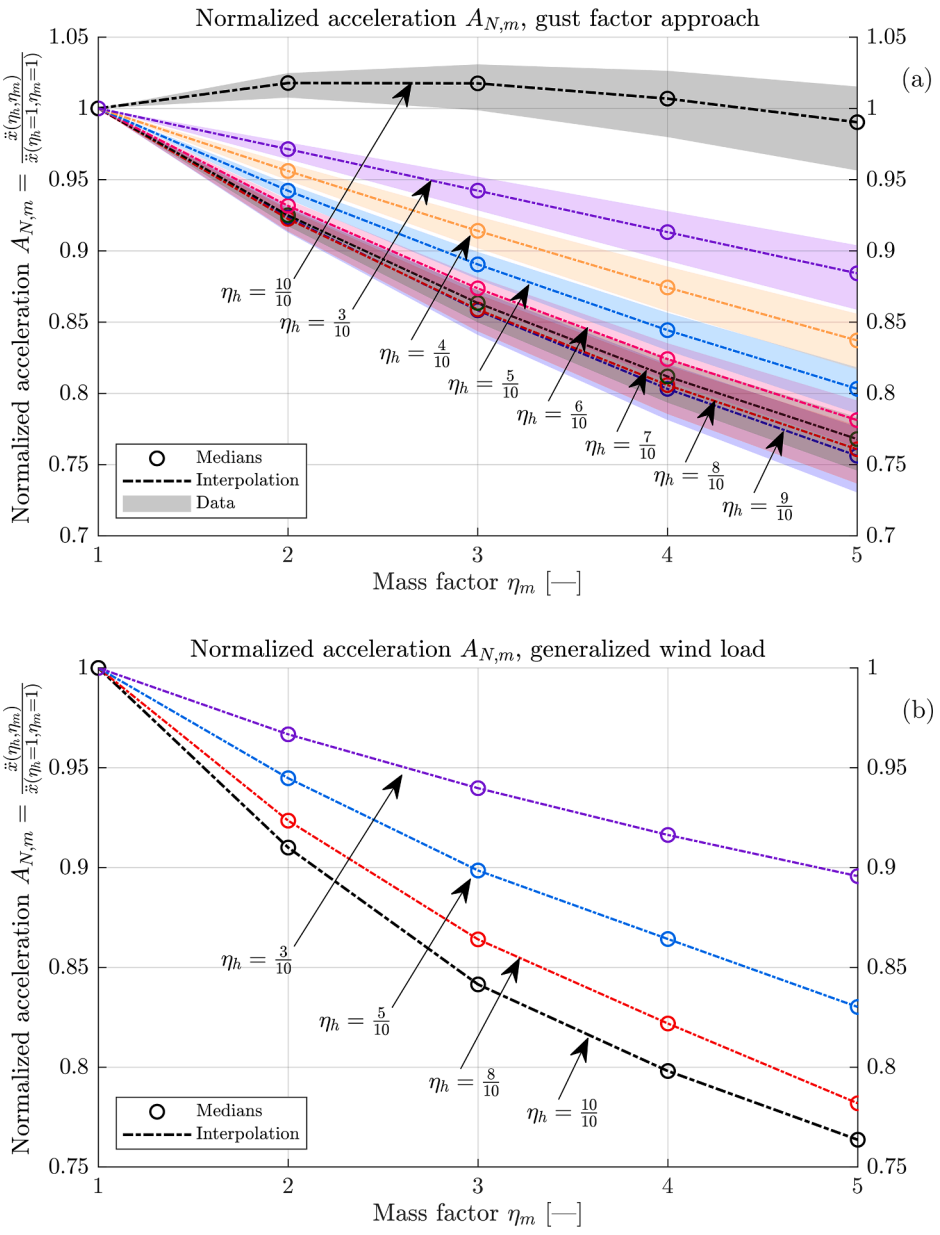

Fig. 13. Normalized acceleration $A_{N,m}$ with respect to the mass factor for a non-uniform mass distribution for **(a)** the gust factor approach, and **(b)** the generalized wind load.

$$x_{GWL} = c_i \frac{\frac{1}{2}\rho_a \bar{u}^2 c_f \left(N_{\text{floor}} H b\right) \left(\frac{L_u}{\sqrt{N_{\text{floor}} H b}}\right)^{5.9}}{N_{\text{bay}}^{0.8} \left(\frac{EI_b}{L_b^3}\right)^{0.1} \left(\frac{EI_c}{H^3}\right)^{0.43} k_\theta^{0.71} k_{x,z,\text{sup}}^{0.05}}, \tag{26b}$$

where c_i is a support coefficient. For the generalized wind load in Equation (26b) the predicted peak displacement is assumed as the 95% percentile for a Gaussian distribution. The support coefficients are given in Table 5. In Equation (26), the mean wind velocity and the geometry are important parameters. The beam stiffness and lateral support stiffness are of less importance. In both expressions, the connections' stiffness has similar exponents and is of high importance. For the gust factor approach, the R^2 is about 0.92. For the generalized wind load, the R^2 is about 0.86.

3.4. Mass distribution

3.4.1. Uniform mass distribution

Fig. 12 shows the effect of increasing the mass of frames uniformly on all floors for the gust factor approach and the generalized wind load. Observe that increasing the mass decreases the accelerations. When the mass factor η_m is 1.0, the surface load is 1.6 kN/m^2. This is the lightest case, and it corresponds to the quasi-permanent load on each floor for a frame spacing of 2.4 m:

$$p_S = g_k + \psi_{2,q} q_k, \tag{27}$$

with a self-weight $g_k = 1$ kN/m^2, live load $q_k = 2$ kN/m^2, and the quasi-permanent factor $\psi_{2,q} = 0.3$. A typical frame with concrete floors will be equivalent to a mass factor η_m between 3.5 and 4.0 in Fig. 12.

Based on the results shown in Fig. 12, frames with heavy floors will have an acceleration that is in the order of 40% lower on average than the lightest timber frame, according to both the gust factor approach and

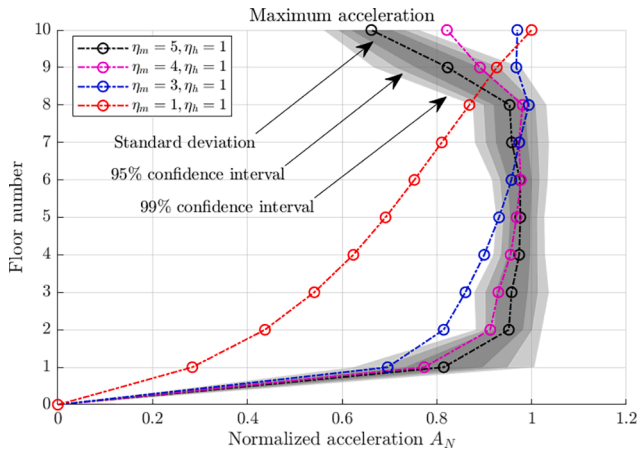

Fig. 14. Accelerations normalized with respect to the maximum frame acceleration for the generalized wind load.

the generalized wind load methods. For the heaviest frame with a surface load of 7 $\mathrm{kN/m^2}$, the reduction in accelerations is more than 50% on average according to the gust factor approach, and more than 60% on average for the generalized wind load approach.

3.4.2. Non-uniform mass distribution

Fig. 13 shows the effect of adding different amounts of mass η_m at different heights η_h for the gust factor approach and the generalized wind load, with the horizontal axis showing the mass factor η_m. The top-floor accelerations are normalized with respect to the reference lightest case, where no additional mass is added. In Fig. 13, all added mass will contribute to reducing the top-floor accelerations independently of the location, except for a height factor η_h of 1.0.

For the gust factor approach in Fig. 13, the optimal location of the mass is surprisingly not at the top floor. Adding mass to the very top of the structure may increase the response top-floor accelerations according to the gust factor approach. The optimal location for the gust factor approach is for a height factor η_h of 0.9 . For a mass factor η_m of 5 and a height factor η_h of 0.9, the median reduction in top-floor acceleration is about 24%. For a mass factor η_m of 2 and a height factor η_h of 0.9, the median reduction in acceleration is about 3%. For the generalized wind load, the optimal location of the mass is at the top floor with a height factor η_h of 1.0. For a mass factor η_m of 5 and a height factor η_h of 1.0, the median reduction in acceleration is about 24%. For a mass factor η_m of 2 and a height factor η_h of 1.0, the median reduction in acceleration is about 9%.

Fig. 13 shows that there is a deviation between the gust factor approach and the generalized wind load. This is the case when the mass is added to the floor of the structure with a height factor η_h of 1.0. A more detailed investigation of this deviation can be found in Cao [38]. Apart from the height factor η_h of 1.0, the gust factor approach and the generalized wind load are in good agreement.

Fig. 14 shows normalized accelerations with respect to the floor number for the generalized wind load. The accelerations are normalized with respect to the maximum acceleration in each floor for different mass factors η_m. For a mass factor η_m of 5 and a height factor η_h of 1.0, the top-floor accelerations are reduced by about 24%. However, the accelerations at mid-height are not reduced as much. From Fig. 14, the maximum acceleration of the frame is located higher for lower mass factors η_m, and lower for higher mass factors. Although the location of the maximum acceleration is shifted, the absolute value of the maximum acceleration is still reduced compared with a uniform mass distribution.

3.4.3. Mode shapes

To investigate the effect of the location of the mass η_h, the mode shapes ϕ_i are evaluated qualitatively. Fig. 15 shows the six first mode shapes ϕ_i for a 10-floor frame with a mass factor $\eta_m = 5$, and a height factor η_h from 0.3 to 1.0. Again, the mode shapes for the reference lightest case with a mass factor η_m of 1.0 are shown in Fig. 15. For the first mode, the lower part of the building in timber structure will in many cases have a more shear-dominated displacement pattern. This is probably due to the limited connection stiffness, especially in the column-to-foundation rotational stiffness.

For the second and third mode shapes ϕ_2 and ϕ_3, the maximum amplitudes are reduced if the mass is located at the peaks of the mode shapes. However, the amplitudes can be reduced even more if the mass is located at slightly different locations. For instance, the second mode shape ϕ_2 can be reduced by a magnitude of about 40% for a height factor η_h of 0.6. For a height factor η_h of 0.3, the peak of the second mode shape ϕ_2 is not reduced as much as for a height factor η_h of 0.6. However, the magnitude of the second mode shape above a normalized height of 0.6 is less severe. For the second and higher modes $\phi_{i\geq 2}$, the amplitudes of the mode shapes are amplified for large height factors η_h. For the second mode shape ϕ_2, height factors above 0.7 result in an amplitude that is almost twice as large as for the uniform mass distribution. For the third mode shape, a height factor η_h of 1.0 gives a maximum amplitude of more than three times that of a uniform mass distribution. For the higher mode shapes, the maximum amplitude is consistently larger for a height factor η_h of 1.0. However, the higher mode shapes are of less importance.

For rigid-like structures such as reinforced concrete and steel buildings, the first mode shape ϕ_1 is often the governing mode shape. In the Eurocodes, only the first mode shape ϕ_1 is used for most buildings. For more flexible structures such as long-span bridges, the inclusion of more mode shapes is necessary to model the dynamic response appropriately. Timber buildings are more flexible and lightweight than rigid-like reinforced concrete and steel buildings, but more rigid than long-span bridges. Thus, the dynamic response of mid- and high- rise timber buildings may necessitate the inclusion of higher modes as their influence is magnified.

The strategic location of mass in timber structures may be a necessity for constructing taller timber structures than today. This strategy can readily be applied to tall timber structures to reduce the dynamic response with active or passive masses. For the 81 m tall timber building Mjøstårnet in Norway, the upper seven floors have 300 mm concrete slabs acting as passive mass [13]. A uniform mass distribution can result in reduced accelerations, as shown in Fig. 12. However, a light structure is desired to reduce the base shear in seismic design. Therefore, a strategic location of added mass on certain floors may be a possible solution.

4. Conclusion

In this paper, the dynamic response of more than one million unique timber frames with moment-resisting beam-to-column connections and different parameters was investigated numerically by Finite Element simulations. The results quantify the theoretical feasibility of frames with respect to wind-induced vibrations under service-load. Two methods was used to study the structural response, namely the gust factor approach and dynamic analysis by use of generated time-history wind loading. Simplified expressions for the fundamental eigenfrequency, the maximum response acceleration, and the maximum response displacement were proposed based on nonlinear regression on the obtained FE results. Moreover, a novel frequency reduction factor was developed. Finally, the effect of uniform and non-uniform mass distributions on the response accelerations was investigated.

The frequency reduction factor shows that there is a sigmoid relationship between the connection stiffness and the fundamental eigenfrequency. For the response accelerations, the gust factor approach may yield nonconservative results compared with the generalized wind load, especially for lighter frames. For a basic wind velocity of 22 m/s and a single-year return period, all the simulated frames satisfy the serviceability criteria of ISO10137 [26]. For the higher wind velocities of

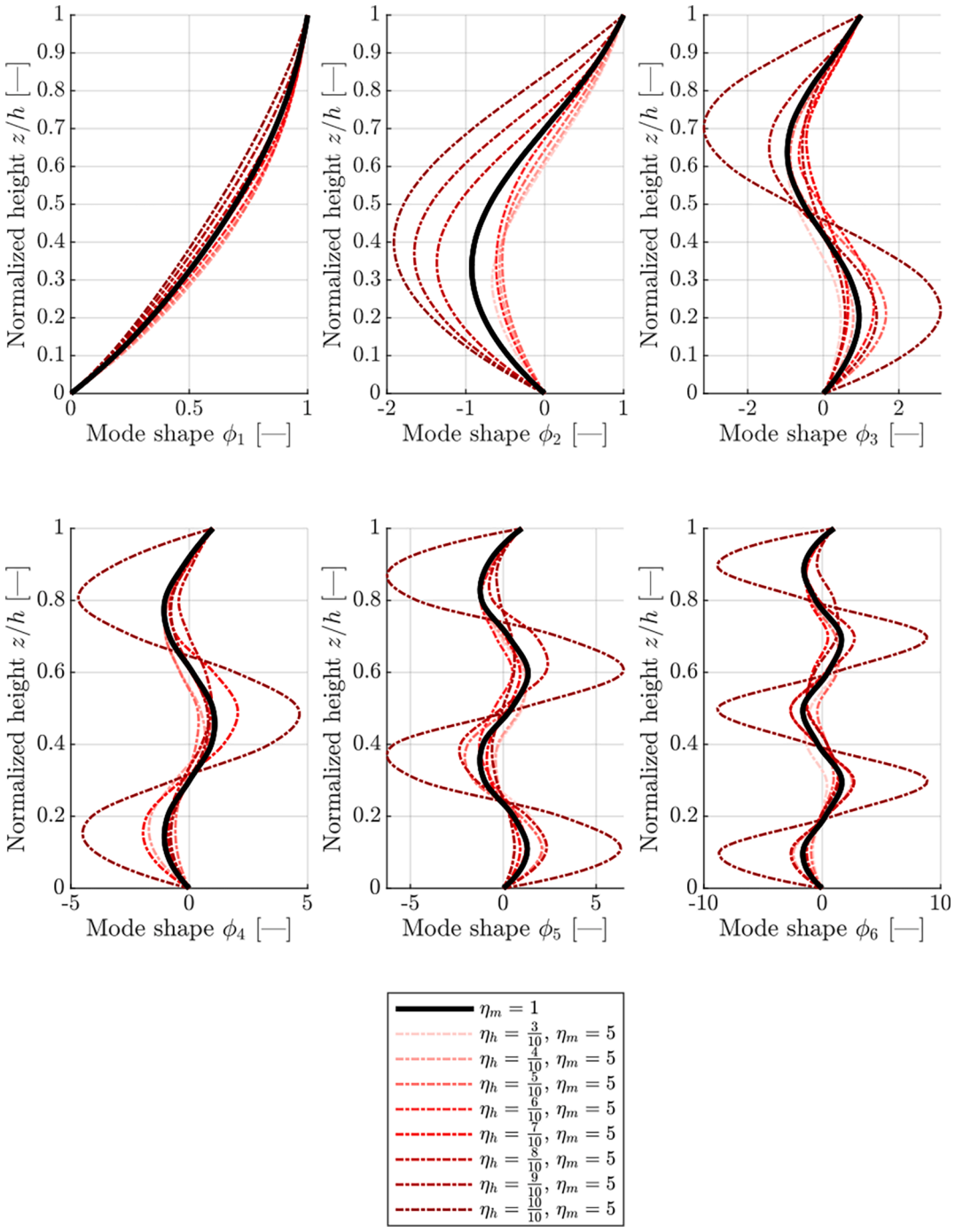

Fig. 15. Mode shapes for various height factors η_h and a mass factor η_m of five.

26 m/s and 30 m/s, most of the simulated semi-rigid frames satisfy the criteria.

The response accelerations can be reduced considerably by uniformly increasing the mass of the frames. If a more mass-efficient method is deemed necessary, non-uniform mass distributions can be applied with additional mass at the top or at intersecting mode shape maxima. By increasing the mass uniformly from 1.6 kN/m^2 to 7 kN/m^2 in terms of surface load per floor area, the top-floor response accelerations can theoretically be reduced by 50% based on median values. For the most favorable non-uniform mass distribution in this paper, the top-floor response accelerations can be reduced by approximately 25%. Although top-floor accelerations were reduced considerably, the location of maximum acceleration was redistributed to other places in the buildings. Thus, introducing a second or third passive mass at strategic points can be beneficial for the overall wind performance of the building.

The proposed nonlinear expressions for the response accelerations, fundamental eigenfrequency, and the frequency reduction factor provide a simplified method for estimating the structural response and properties. The results presented in this paper show that semi-rigid frames are theoretically feasible for buildings with up to 10 floors with uniform mass distributions. For non-uniform mass distributions, even taller structures complying with the serviceability criteria can be designed and built.

A major limitation and topic for future work is the experimental validation of the numerical results in this paper. Special attention should

be given to the discrepancy between the two numerical methods used in this paper to assess the dynamic response of timber structures. Other future work include similar analyses for other types of timber buildings such as CLT buildings, hybrid buildings with concrete cores, braced systems and more.

Declaration of Competing Interest

The authors declare that they have no known competing financial interests or personal relationships that could have appeared to influence the work reported in this paper.

Acknowledgements

The work reported in this paper was made possible by the computing power provided by the private company Nordic Group Holding AS. This generous support is much appreciated. This article has been written in the framework of the Woodsol project, which is funded by the Research Council of Norway, Norway (NFR grant no. 254699/E50).

Credit author statement

Both authors have seen and approved the manuscript and have contributed significantly to its preparation. Both authors have contributed significantly to the conceptual development of the topic. The 1st author has written the manuscript (including figure preparation), developed the MATLAB routines for the wind loading and the dynamic analysis of the frames, and has performed all calculations (in frequency- and time- domain). The 2nd author has developed the Finite Element formulation of the frames in MATLAB and has critically reviewed the manuscript.

References

[1] Ceccotti A, Sandhaas C, Okabe M, Yasumura M, Minowa C, Kawai N. SOFIE project – 3D shaking table test on a seven-storey full-scale cross-laminated timber building. Earthquake Eng Struct Dyn 2013;42:2003–21.
[2] Pei S, Van de Lindt J, Barbosa AR, Berman J, Blomgren H-E, Dolan J, et al. Full-scale shake table test of a two-story mass-timber building with resilient rocking walls. 16th European Conference on Earthquake Engineering. Thessaloniki, Greece. 2018.
[3] Reynolds T, Harris R, Chang W, Bregulla J, Bawcombe J. Ambient vibration tests of a cross-laminated timber building. Constr Mater 2015;168:121–31.
[4] Auersch L. Simple and fast prediction of train-induced track forces, ground and building vibrations. Railway Eng Sci 2020;28:232–50.
[5] Persson P, Andersen LV, Persson K, Bucinskas P. Effect of structural design on traffic-induced building vibrations. Procedia Eng 2017;199:2711–6.
[6] Huang H, Gao Y, Chang W-S. Human-induced vibration of cross-laminated timber (CLT) floor under different boundary conditions. Eng Struct 2020;204:110016.
[7] Weckendorf J, Toratti T, Smith I, Tannert T. Vibration serviceability performance of timber floors. Eur J Wood Wood Prod 2016;74:353–67.
[8] Bezabeh MA, Bitsuamlak GT, Popovski M, Tesfamariam S. Dynamic Response of Tall Mass-Timber Buildings to Wind Excitation. J Struct Eng 2020;146:04020199.
[9] Edskär I, Lidelöw H. Wind-Induced Vibrations in Timber Buildings—Parameter Study of Cross-Laminated Timber Residential Structures. Struct Eng Int 2017;27:205–16.
[10] Abrahamsen R, Malo KA. Structural design and assembly of "Treet" - A 14-storey timber residential building in Norway. WCTE2014 World Conference of Timber Engineering. Quebec City, Canada. 2014.
[11] Johansson ML, Andreas Jarnerö K, Landel P. Tall timber buildings - A preliminary study of wind-induced vibrations of a 22-storey building. WCTE 2016, World Conference on Timber Engineering. Vienna, Austria. 2016.
[12] Malo KA, Stamatopoulos H. Connections with threaded rods in moment resisting frames. WCTE 2016, World Conference on Timber Engineering. Vienna, Austria. 2016.
[13] Abrahamsen R. Mjøstårnet - Construction of an 81 m tall timber building. Internationales Holzbau-Forum IHF 2017.
[14] Malo KA, Abrahamsen R, Bjertnæs MA. Some structural design issues of the 14-storey timber framed building "Treet" in Norway. Eur J Wood Wood Prod 2016;74:407–24.
[15] Stamatopoulos H, Malo KA. Wood frame solutioons for free space design in urban buildings (WOODSOL). 7th Forum Wood Building Nordic Växjö 18. Växjö, Sweden. 2018.
[16] Vilguts A, Malo KA, Stamatopoulos H. Moment resisting frames and connections using threaded rods in beam-to-column timber joints. WCTE 2018, World Conference on Timber Engineering. Seoul, Republic of Korea. 2018.
[17] Stamatopoulos H, Malo KA. Withdrawal stiffness of threaded rods embedded in timber elements. Constr Build Mater 2016;116:263–72.
[18] Bjørge H, Kristoffersen T. Konseptstudie av trebaserte kompositttdekker med mulighet for innspenning til limtresøyler. Trondheim: NTNU; 2017.
[19] Fragiacomo M, Batchelar M. Timber Frame Moment Joints with Glued-In Steel Rods. I: Design. J Struct Eng 2012;138:789–801.
[20] Leijten AJ, Ruxton S, Prion H, Lam F. Reversed-Cyclic Behavior of a Novel Heavy Timber Tube Connection. J Struct Eng 2006;132:1314–9.
[21] van Bakel R, Rinaldin G, Leijten AJM, Fragiacomo M. Experimental–numerical investigation on the seismic behaviour of moment-resisting timber frames with densified veneer wood-reinforced timber joints and expanded tube fasteners. Earthquake Eng Struct Dyn 2017;46:1307–24.
[22] Komatsu K. Development of stiffer and ductile glulam portal frame. AIP Conf Proc 2017;1903:020026.
[23] Chen Z, Popovski M, Gerber A. Seismic performance of post-tensioned moment-resisting portal frames. WCTE 2018, World Conference on Timber Engineering. Seoul, Republic of Korea. 2018.
[24] Vilguts A, Stamatopoulos H, Malo KA. Parametric analysis and feasibility studies of moment-resisting timber frames under service load. Eng Struct 2021;228.
[25] CEN ECfS. Eurocode 1: Actions on structures. Part 1-4: General actions, Wind actions; 2005.
[26] ISO. ISO 10137-2007. Bases for design of structures - Serviceability of buildings and walkways against vibrations; 2007.
[27] CEN ECfS. Eurocode 8: Design of structures for earthquake resistance. Part 1: General rules, seismic actions and rules for buildings; 2004.
[28] Norge S. NS-EN 1991-1-4:2005+NA: 2009 Eurocode 1: Actions on Structures. Part 1-4: General actions, Wind actions Norway: Standard Norge; 2005.
[29] Lui EM, Lopes A. Dynamic analysis and response of semirigid frames. Eng Struct 1997;19:644–54.
[30] Awkar JC, Lui EM. Seismic analysis and response of multistory semirigid frames. Eng Struct 1997;21:425–41.
[31] Feldmann A, Huang H, Chang W, Harris R, Dietsch P, Gräfe M, et al. Dynamic properties of tall timber structures under wind-induced vibration. WCTE 2016, World Conference on Timber Engineering. Vienna, Austria. 2016.
[32] Aloisio A, Pasca D, Tomasi R, Fragiacomo M. Dynamic identification and model updating of an eight-storey CLT building. Eng Struct 2020;213:110593.
[33] Reynolds T, Casagrande D, Tomasi R. Comparison of multi-storey cross-laminated timber and timber frame buildings by in situ modal analysis. Constr Build Mater 2016;102:1009–17.
[34] Abrahamsen R, Bjertnæs MA, Bouillot J, Brank B, Cabaton L, Crocetti R, et al. Dynamic response of tall timber buildings under service load - the DynaTTB research program. In: Eurodyn 2020. Athens, Greece; 2020. p. 4900–10.
[35] Kaimal JC, Wyngaard JC, Izumi Y, Coté OR. Spectral characteristics of surface-layer turbulence. Q J R Meteorolog Soc 1972;98:563–89.
[36] Davenport AG. The application of statistical concepts to the wind loading of structures. Proc Inst Civ Eng 1961;19:449–72.
[37] Kareem A. Synthesis of Fluctuating along Wind Loads on Buildings. J Eng Mech 1986;112:121–5.
[38] Cao AS. The dynamic response of semi-rigid timber frames subjected to dynamic wind loads [Thesis]. Trondheim: Norwegian University of Science and Technology; 2020.
[39] Shinozuka M, Deodatis G. Simulation of Stochastic Processes by Spectral Representation. Appl Mech Rev 1991;44:191–204.
[40] CEN ECfS. EN 14080 Timber structures. Glued laminated timber and glued solid timber – Requirements; 2013.
[41] Irwin PA. Vortices and tall buildings: A recipe for resonance. Phys Today 2010;63:68–9.
[42] CEN ECfS. Eurocode 0: Basis of structural design; 2002.
[43] Davenport AG. The spectrum of horizontal gustiness near the ground in high winds. Q J R Meteorolog Soc 1961;87:194–211.
[44] Davenport AG. The treatment of wind loading on tall buildings. Tall Build 1967:3–45.
[45] Davenport AG. Note on the distribution of the largest value of a random function with application to gust loading. Proc Inst Civ Eng 1964;28:187–96.
[46] Kareem A, Hu L, Guo Y, Kwon D-K. Generalized Wind Loading Chain: Time-Frequency Modeling Framework for Nonstationary Wind Effects on Structures. J Struct Eng 2019;145:04019092.
[47] Solari G. Gust Buffeting. I: Peak Wind Velocity and Equivalent Pressure. J Struct Eng 1993;119:365–82.
[48] Solari G. Gust Buffeting. II: Dynamic Alongwind Response. J Struct Eng 1993;119:383–98.
[49] Solari G. Equivalent Wind Spectrum Technique: Theory and Applications. J Struct Eng 1988;114:1303–23.
[50] Solari G, Kareem A. On the formulation of ASCE7-95 gust effect factor. J Wind Eng Ind Aerodyn 1998;77–78.
[51] Steenbergen RDJM, Vrouwenvelder ACWM, Geurts CPW. The use of Eurocode EN 1991-1-4 procedures 1 and 2 for building dynamics, a comparative study. J Wind Eng Ind Aerodyn 2012;129:103–6.